*Journal of Metals, Materials and Minerals, Vol. 33, No. 1, pp. 89-94, 2023*

# Fabrication of glass-ceramics composite by infiltration of lithium tetraborate glass into porous magnesium aluminate spinel ceramic

Nattawat KULRAT[1,*], Chumphol BUSABOK[2], Saweat INTARASIRI[3], Somsak DANGTIP[1,4,*], and Wasana KHONGWONG[2]

[1] *Department of Physics and Nanotec CoE at Mahidol University, Faculty of Science, Mahidol University, Bangkok, 10400, Thailand*
[2] *Expert Centre of Innovative Materials, Thailand Institute of Scientific and Technological Research (TISTR) Pathum Thani, 12120, Thailand*
[3] *Science and Technology Research Institute, Chiang Mai University, Chiang Mai, 50200, Thailand*
[4] *Thailand Institute of Nuclear Technology, Nakhon Nayok, 26120, Thailand*

***Corresponding author e-mail:** nattawat1729@gmail.com; somsakd@tint.or.th

**Received date:**
22 September 2022
**Revised date**
8 January 2023
**Accepted date:**
18 January 2023

**Keywords:**
Glass-ceramics composite;
Glass infiltration;
Lithium tetraborate glass;
Magnesium aluminate spinel;
Porous

**Abstract**

Magnesium aluminate spinel (MAS) glass-ceramics composite has excellent mechanical and optical properties. It can be obtained from porous ceramic by infiltrating the proper choice of glass. In this study, porous MAS ceramic was prepared by conventional sintering from MAS powder to reach a bulk density of 2.48 g·cm$^{-3}$ (70.1% of relative density). The porous MAS ceramic was then infiltrated with molten lithium tetraborate glass ($Li_2B_4O_7$; LTB) at 950°C for 30 (IF30) and 60 (IF60) min. They were left to cool down to 700°C inside the furnace before being taken out to quench in ambient. The glass-ceramics composite was obtained with 98.7% and 92.1% relative density for IF30 and IF60 cases, respectively. SEM images reveal a lower degree of porosity in the IF30 case, which achieves higher flexural strength of 119.7 MPa. X-ray diffraction and Raman spectroscopy indicate that $Mg_2B_2O_5$ phase (at $2\theta$=35°) and $B_2O_5$ functional group (at 847 cm$^{-1}$) are formed during infiltration. Consequently, their micro vickers hardness increased (3.41→5.53→6.16 GPa).

## 1. Introduction

Highly dense magnesium aluminate spinel ($MgAl_2O_4$; MAS) is classified as transparent ceramics [1,2]. It has potential for application in various fields due to its excellent properties, e.g., high mechanical strength [2,3], low thermal expansion [4], chemical inertness, and high transparency from near-UV to mid-IR [4,5], etc. Highly dense MAS are typically fabricated using pressure-assisted sintering methods, e.g., spark plasma sintering (SPS) [4], microwave sintering and hot isostatic press (HIP) [5,6] from a nano-size of MAS powder [7,8]. Generally, the large particle size (micron-size) cannot achieve high relative density by conventional sintering, which is classified as a porous ceramic and shows inferior properties. However, there are alternative routes to producing high relative density composites by adding other matrices, such as glass-ceramics composite [9,10] and polymer-ceramics composite [11,12]. Although the composite properties are not comparable to the highly dense MAS, it can be applied in other appropriate features. In-Ceram Spinell (VITA-Germany) [13] is a notorious example of MAS glass-ceramics composite. It started by machining porous MAS (relative density ~70%) to the desired shape by computer-aided design and computer-aided manufacturing (CAD/CAM) [14], then it was infiltrated with lanthanum-rich glass ($La_2O_3$–$Al_2O_3$–$SiO_2$). The MAS glass-ceramics composite was applied as esthetic dental restorative material, e.g., anterior teeth and veneer by its excellent properties in flexural strength, hardness, colour, and translucency [9,15]. In addition, the low shrinkage (near-net-shape) of glass infiltrated samples is a special feature of this product.

Glass infiltration is a promising technique that applies molten glass infiltration into a consolidated porous medium [16,17]. The composite consists of glass and crystalline matrixes that obtain high relative density, which significantly improves the mechanical and optical properties. Residual porosity is the main problem that significantly affects the properties of the composite. It can be created by the low uniformity of pore size of porous ceramics, gas trapped in the glass matrix, the shrinkage of the glass matrix upon cooling [18,19], etc. To solve these problems, the glass matrix should have low reactivity, similar density and thermal expansion to the ceramic matrix [18,19]. Therefore, lanthanum-rich glass is widely used to infiltrate porous MAS ceramic due to its appropriate properties as mentioned. However, there have not been many studies about using other glass to infiltrate porous MAS.

This work aimed to fabricate dense glass-ceramics composite by infiltration of lithium tetraborate glass ($Li_2B_4O_7$; LTB) into porous MAS ceramic. The LTB glass can react with MAS and improve the properties of porous MAS ceramic. The processing parameters that affected the properties of the composite were investigated.

## 2. Experimental

### 2.1 Fabrication of porous MAS ceramic

The MAS powder was synthesized by solid-state reaction of $\alpha$-$Al_2O_3$ (high purity, Sigma Aldrich) and $Mg(OH)_2$ (high purity, Daejung, Korea) powders. The composition was varied the molar ratio of MgO:$Al_2O_3$ by 1:1. The mixture was homogenized by planetary ball milling in a plastic container with ethanol medium and alumina ball at a frequency of 240 rpm for 24 h. Then the slurry was dried at 100°C for 24 h. The homogenized powder was calcined in ambient with heating rate of 5°C·min$^{-1}$ from room temperature to 1400°C and kept soaking time for 5 h, then it was left to cool down in the furnace. The MAS powder was sieved with #325 mesh. It has median particle size 3.6 µm which was analyzed by laser diffraction particle size analyzer (Mastersizer 3000, Malvern Panalytical). Porous MAS ceramic was fabricated by conventional sintering from a MAS powder. The powder was pressed by uniaxial pressing at 2 tons to a cylindrical shape, then it was compacted by cold isostatic pressing (CIP, Kobelco, Japan) with a control pressure of 200 MPa for 5 min. The green bodies were sintered at a heating rate of 5°C·min$^{-1}$ to 1600°C. It was soaked at this temperature for 5 h, then left to cool down to room temperature in the furnace. The sintered sample is porous ceramic, which has a cylindrical shape of 22 mm in diameter and 16 mm in thickness.

### 2.2 Glass infiltration

LTB glass powder (High purity, Alfa Aesar, USA) was ground by a vibratory ring mill for 15 min and sieved through an #80 mesh sieve to select particles size <180 µm. Glass powder was pressed at a load of 2 tons to be a pellet shape with 22 mm in diameter and 2 mm in thickness (for 2.5 g of glass powder) and put on top of porous MAS ceramic as illustrated in Figure 1(a) then kept together in a melting furnace to heat up to 950°C at a heating rate of 6°C·min$^{-1}$. At this temperature, molten glass can gravitate from the top to bottom part of porous MAS ceramic. Infiltration time was controlled by 30 min and 60 min as denoted by IF30 and IF60 samples, respectively. After the infiltration process, the sample was cooled down to 700°C inside the furnace, then it was immediately taken outside the furnace for quenching to room temperature. The infiltrated sample is shown in Figure 1(b).

### 2.3 Sample preparation and Characterization

The sample was cut vertically by a high-precision cutting machine (Buehler IsoMet), which resulted in a cross-section specimen with a size ~9.0 mm × 20.0 mm ×2.5 mm. (width × length × thickness) as shown in Figure 1(c). This cross-section specimen will be used in the measurement of density, X-ray diffraction (XRD), Raman spectroscopy, and scanning electron microscopy (SEM). The cross-section specimen was cut to a bar shape with a size ~2.5 mm × 2.5 mm × 20.0 mm. (width × thickness × length) as shown in Figure 1(d), then they were tested for three-points flexural strength and micro vickers hardness. The density of the sample was determined by using the Archimedes method. Apparent density ($\rho_A$), bulk density ($\rho_B$), and relative density (R.D.) were calculated by the following equations [20].

$$\rho_A = [m_1 / (m_1 - m_3)] \times \rho_w \quad (1)$$

$$\rho_B = [m_1 / (m_2 - m_3)] \times \rho_w \quad (2)$$

$$R.D. = [\rho_B / \rho_A] \times 100\% \quad (3)$$

Where $\rho_w$ is the density of distilled water, $m_1$ is dry mass, $m_2$ is immersed mass after boiling in distilled water for 2 h and soaking further for 12 h, and $m_3$ is mass as weighting in distilled water. The flexural strength (σ) of a bar shape specimen was measured by three-point flexural test and it was calculated by the following equation.

$$\sigma = 3FL / 2bd^2 \quad (4)$$

Where $F$, $L$, $b$, and $d$ are the weight of load at the fracture point, length of support span, sample width, and sample thickness, respectively. Micro vickers hardness ($H_v$) was tested by micro hardness testing machine (HM-200 Mitutoyo, Japan) under indenter load of 0.3 kg and it was calculated by the following equation.

$$H_v = 1.854P / a^2 \quad (5)$$

Where $P$ is the weight of the load (2.942 N) and $a$ is the average of the diagonal lengths of the indentation. The indentation was performed at five points for each specimen. Furthermore, the density, flexural strength, and micro vickers hardness measurements were performed with 4 samples for each condition. The average and standard deviation values were reported.

The morphologies of the cross-section specimens were revealed by scanning electron microscope (SEM; JEOL-JSM 5400, Japan) at ×1000, ×5000, and ×10000 magnification. Crystallographic phase identification was carried out by X-ray diffraction (XRD, Malvern Panalytical Aeris) using CuK$\alpha$ radiation (0.15406 nm). The scanning length of the diffraction angle was 15.0000° to 65.0000° and the step size was 0.0217°. Raman spectra were measured by Laser Raman spectroscopy (RAMAN force, NanoPhoton) with 532 nm of wavelength and a beam width of 3 µm.

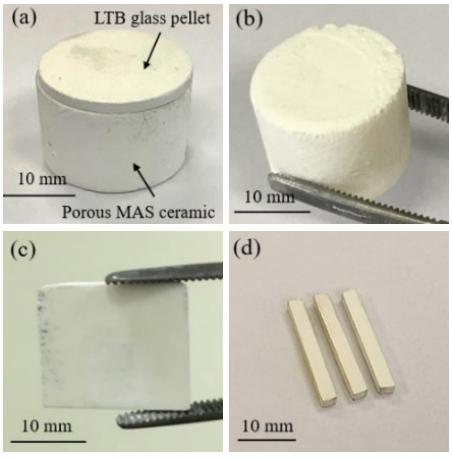


**Figure 1.** Sample preparation (a) the arrangement of porous MAS ceramic and LTB glass pellet before glass infiltration process, (b) glass infiltrated sample, (c) cross-section specimen, and (d) bar-shaped specimens.

## 3. Results and discussion

### 3.1 Physical properties

Table 1 reveals the physical properties of porous MAS ceramic and MAS glass-ceramics composite sample. Porous MAS ceramic has R.D.≈70%. Therefore, it has a porosity of 30% by volume. When the glass infiltrated into pore space, the apparent density of infiltrated sample ($\rho_i$) can be estimated by the following equation [21].

$$\rho_i = 0.30_{\rho_g} + 0.70_{\rho_{MAS}} \quad (6)$$

Where $\rho_g$ (2.42 g·cm$^{-3}$) is apparent density of LTB glass and $\rho_{MAS}$ (3.54 g·cm$^{-3}$) is apparent density of MAS. Consequently, the apparent density of the completely infiltrated sample is estimated to be 3.20 g·cm$^{-3}$. The apparent density of IF30 (3.14 g·cm$^{-3}$) is greater than IF60 (3.05 g·cm$^{-3}$) but it is still lower than the estimation value. The reduction in apparent density indicates that the glass matrix lowers its density with increasing infiltration time. However, another factor is glass shrinkage upon cooling that can affect the unit cell of MAS and porosity [22,23]. The flexural strength of IF30 sample increased from porous MAS ceramic, while the opposite was found in the case of IF60. Moreover, the micro vickers hardness is improved from porous MAS ceramic when increased infiltration time.

### 3.2 XRD results

Figure 2(a) presents the XRD pattern of MAS porous ceramics, IF30, and IF60. From main diffraction peaks of all samples could be identified that MAS (JCPDS number 21-1152) was the major phase. The intensity of the MAS pattern from IF60 obviously decreased as compared with IF30. It was also found that the predominant peak at the reflecting plane (311) shifted to a higher diffraction angle and broadened in IF60. The comparison of Gaussian fitting information of the peak at the reflecting plane (311) is presented in Table 2. There is a very similar peak area between IF30 and IF60 but lower than MAS porous because the amorphous structure from glass matrix overlay covers the MAS porous which make the XRD signal from crystalline phase dropped. In addition, the broaden peak from IF60 refers to a non-uniformly lattice strain of MAS while the case of IF30 has a sharp peak which corresponds to the uniform lattice strain of MAS. The calculation of lattice strain ($\varepsilon_{311}$) at the plane (311) of MAS by using the MAS porous as reference as shown in Table 2, IF60 has a compressive strain of 0.14% while IF30 has a tensile strain of 0.06%. Furthermore, the enlargement plotting at diffraction angle 2$\theta$ between 20° to 44°of MAS porous ceramic, IF30, and IF60 are shown in Figure 2(b). They show the phase formation of $Mg_2B_2O_5$ (JCPDS number 15-0537) and α-$Al_2O_3$ (JCPDS number 71-1123) which can be described the reaction by the following.

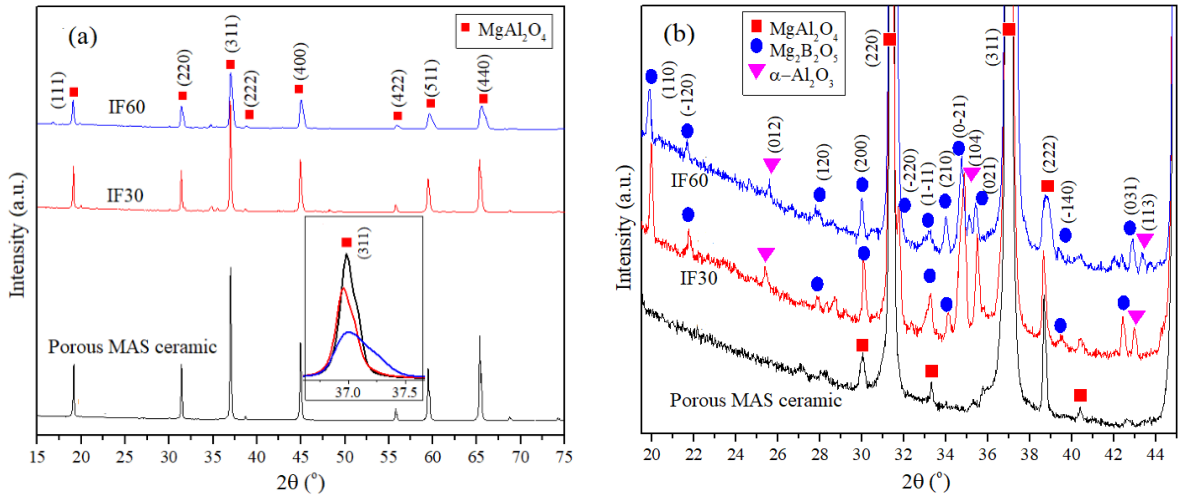


**Figure 2.** XRD patterns of porous MAS ceramic, IF30, and IF60 at diffraction angle 2$\theta$ between (a) 15° to 75° and (b) 20° to 44°.

**Table 1**. The mean and standard deviation values of bulk density ($\rho_B$), apparent density ($\rho_A$), relative density (R.D.), flexural strength (σ), and micro vickers hardness (HV).

| Sample | $\rho_B$ (g·cm$^{-3}$) | $\rho_A$ (g·cm$^{-3}$) | R.D. (%) | σ (MPa) | $H_V$ (GPa) |
|---|---|---|---|---|---|
| Porous MAS ceramic | 2.48 ± 0.02 | 3.54 ± 0.01 | 70.06 ± 0.01 | 111.8 ± 1.4 | 3.41 ± 0.05 |
| IF30 | 3.10 ± 0.02 | 3.14 ± 0.04 | 98.73 ± 0.02 | 119.7 ± 8.3 | 5.53 ± 0.10 |
| IF60 | 2.81 ± 0.01 | 3.05 ± 0.01 | 92.13 ± 0.01 | 102.6 ± 9.0 | 6.16 ± 0.20 |

**Table 2.** The details of Gaussian fitting of peak (311) and the calculation of strain value ($\varepsilon_{311}$) of MAS phase obtained from XRD results.

| Sample | 2$\theta$ (deg) | FWHM (deg) | Intensity(a.u.) | Area(a.u.) | $d_{311}$(Å) | $\varepsilon_{111}$(%) |
|---|---|---|---|---|---|---|
| Porous MAS ceramic | 37.0003 | 0.1819 | 100136.45 | 19389.77 | 2.4267 | none |
| IF30 | 36.9757 | 0.2038 | 73931.38 | 16036.55 | 2.4282 | 0.06 |
| IF60 | 37.0550 | 0.3977 | 38732.58 | 16325.25 | 2.4232 | -0.14 |

$$Li_2B_4O_7 \rightarrow Li_2O + 2B_2O_3 \quad (7)$$

$$2MgAl_2O_4 + B_2O_3 \rightarrow Mg_2B_2O_5 + 2Al_2O_3 \quad (8)$$

LTB glass can transform into $Li_2O$ and $B_2O_3$ at 950°C, corresponding to Equation (7). The $Li_2O$ can vaporize due to the temperature being greater than its melting point, thus only $B_2O_3$ can react with MAS by following Equation (8). The production of $Mg_2B_2O_5$ and $Al_2O_3$ has a low content as compared to MAS because this reaction may only be at the surface of MAS particles [24]. In the case of IF30, the glass matrix is not fully attached with MAS. The glass matrix can shrink in the direction away from MAS during the quenching process, thus tensile strain was introduced at the MAS unit cell. While IF60 has more time for attachment between glass matrix and MAS. Moreover, the $Mg_2B_2O_5$ can accumulate at the surface of MAS with a chance to interstitial at MAS that affects the compressive strain on the MASunit cell and resulting in an increase of micro vickers hardness.

### 3.3 Raman spectra results

Raman spectra of all samples are shown in Figure 3. The infiltrated sample did not show the Raman peak at 772 $cm^{-1}$ which was attributed to the six-membered borate ring with one and two $BO_4$ units from LTB glass [25], indicating that LTB glass deforms at 950°C. The vibrational mode from MAS consists of $T_{2g(1)}$ (301 $cm^{-1}$), $E_g$ (403 $cm^{-1}$), $T_{2g(2)}$ (667 $cm^{-1}$), $A_{1g}$ (763 $cm^{-1}$) and $AlO_4$ (719 $cm^{-1}$) [26]. The lattice vibration from $Mg_2B_2O_5$ reveals the peaks at, 206, 236, 289, and 480 $cm^{-1}$ [27]. The major peak at 847 $cm^{-1}$ is scissor bending vibration in a pyroborate unit ($B_2O_5$) [27] from $Mg_2B_2O_5$ and glass matrix. In addition, the vibrational at 1281 $cm^{-1}$ corresponds to the asymmetric stretching vibration of the B-O bond in $BO_3$ [28] from the glass matrix. Therefore, after the deformation of LTB, the B-O molecule will connect to a high degree of network and mostly has a pyroborate unit. The Raman peak of lattice vibrational modes of $Mg_2B_2O_5$ disappears at IF60, which according to the XRD results in a lower intensity of $Mg_2B_2O_5$ peak.

### 3.4 Microstructure

Figure 4(a) reveals the microstructure of porous MAS. It has low uniformity of pore size due to the large particle size of MAS powder and using the conventional sintering process, thus MAS porous can reach the relative density only of 70.06%. The microstructure of IF30 has the elimination of surface-connected porosity as shown in Figure 4(b), which supports the improvement of relative density and mechanical properties. While in the case of IF60, it can be observed the rough surface and remaining closed pore as shown in Figure 4(c) which significantly affect the dropping of flexural strength [29]. The appearance of closed pore signifies that the glass may flow out of the porous medium when the infiltration time was excessive. The other factor is $Li_2O$(g) from LTB glass could accumulate and it was trapped inside the composite after quenching process because the specimen was suddenly cooled from the outside to the inside region.

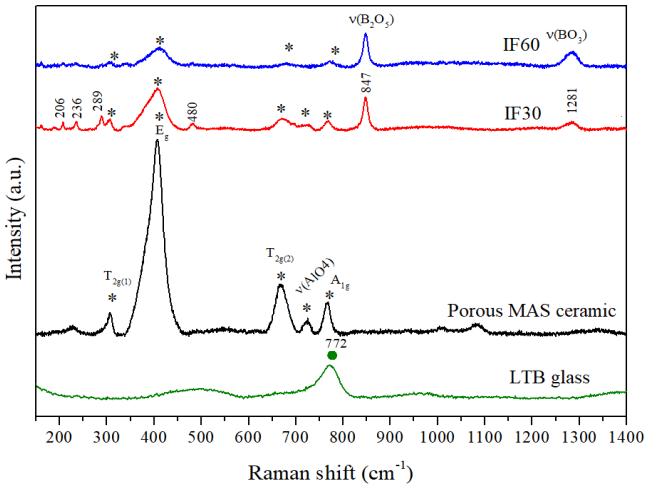


**Figure 3.** Raman spectra of LTB glass, porous MAS ceramic, IF30, and IF60.

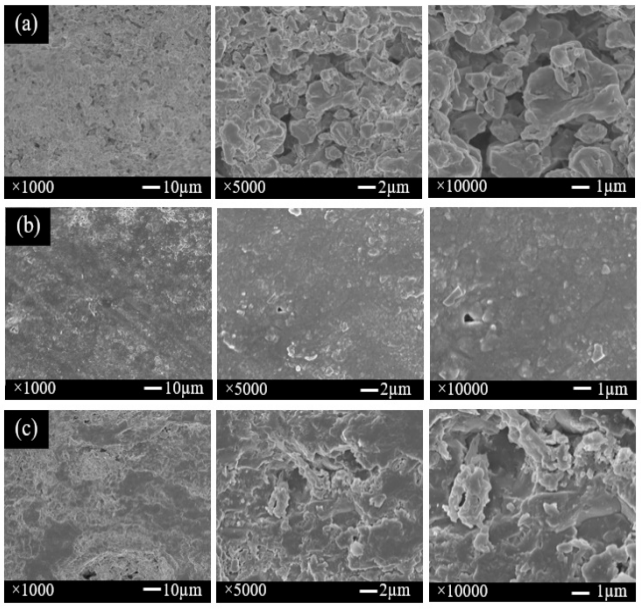


**Figure 4.** SEM images at ×1000, ×5000, and ×10000 of magnification of (a) porous MAS ceramic, (b) IF30, and (c) IF60.

## 4. Conclusions

This work was successful in fabricating dense glass-ceramics composite by infiltration of LTB glass into porous MAS. The optimum infiltration time for 30 min (IF30) shows a completely infuse by the relative density of the composite is 98.73% and shows the improvement of flexural strength and micro vicker hardness while prolonging of infiltration time for 60 min (IF60) has remained of the closed pore that affected the reduction in flexural strength. The molten LTB glass can partially be transformed to $B_2O_3$ and slightly react with the MAS particle which shows the production of $Mg_2B_2O_5$. Hypothetically, the interstitial of $Mg_2B_2O_5$ at the interface of MAS particles shows the compressive stress on the MAS unit cell, resulting in higher micro vickers hardness.

## Acknowledgements

This work has financial support from the Development and Promotion of Science and Technology Talents Project (DPST). The laboratory equipment was supported by Thailand Institute of Scientific and Technological Research (TISTR).

## References

[1] P. Biswas, R. Johnson, Y. R. Mahajan, and G. Padmanabham, "Processing of infrared transparent magnesium aluminate spinel: an overview," *Handbook of Advanced Ceramics and Composites: Defense, Security, Aerospace and Energy Applications*, pp. 495-531, 2020.

[2] A. Goldstein, and A. Krell, "Transparent ceramics at 50: Progress made and further prospects," *Journal of the American Ceramic Society*, vol. 99, no. 10, 3173-3197, 2016.

[3] I. Ganesh, "A review on magnesium aluminate ($MgAl_2O_4$) spinel: synthesis, processing and applications," *International Materials Reviews,* vol. 58, no. 2, pp. 63-112, 2013.

[4] D. C. Harris, L. Johnson, R. Seaver, T. Lewis, G. Turri, M. Bass, and N.D. Haynes, "Optical and thermal properties of spinel with revised (increased) absorption at 4 to 5 μm wavelengths and comparison with sapphire," *Optical Engineering*, vol. 52, no. 8, pp. 087113-087113, 2013.

[5] T. J. Mroz, T. M. Hartnett, J. M. Wahl, L. M. Goldman, J. Kirsch, and W. R. Lindberg, "Recent advances in spinel optical ceramic," In Window and Dome Technologies and Materials IX, *International Society for Optics and Photonics*, pp. 64-70, 2005.

[6] R. Sarkar, and S. Sahoo. "Effect of raw materials on formation and densification of magnesium aluminate spinel," *Ceramics International,* vol. 40, no. 10, pp. 16719-16725, 2014.

[7] K. Morita, B. N. Kim, H. Yoshida, and K. Hiraga, "Densification behaviour of a fine-grained $MgAl_2O_4$ spinel during spark plasma sintering (SPS)," *Scripta Materialia63,* vol. 6, pp. 565-568, 2010.

[8] D. S. Tsai, C. T. Wang, S. J. Yang, and A. S. Hsu, "Hot isostatic pressing of $MgAl_2O_4$ spinel infrared windows," *Material and manufacturing process*, vol. 9, no. 4, pp. 709-719, 1994.

[9] P. C. da Silva, R. de Oliveira Magnago, F. de Assis Baiao Miranda Pereira, K. Strecker, B. Galvao Simba, and C. dos Santos, "Magnesium aluminate spinel ceramics infiltrated with lanthanum-glass for dental applications," *International Journal of Materials Research*, vol. 110, no. 9, pp. 885-891, 2019.

[10] R. D. O. Magnago, F. D. A. B. Miranda Pereira, P. C. da Silva, J. V. C. de Souza, and C. dos Santos, "Infiltrated spinel-based ceramic ($MgAl_2O_4$) for dental application," *Materials Science Forum, Trans Tech Publications*, vol. 881, 2017.

[11] D. Kumar, A. Moharana, and A. Kumar, "Current trends in spinel based modified polymer composite materials for electro-magnetic shielding," *Materials Today Chemistry*, vol. 17, p. 100346, 2020.

[12] E. Elhomiamy, Y. Aboushady, and B. El Malakh, "Wear behaviour and surface roughness of polymer infiltrated ceramic material compared to pressable glass-ceramic," *Alexandria Dental Journal*, vol. 40, no. 1, pp. 65-70, 2015.

[13] P. Magne, and U. Belser. "Esthetic improvements and in vitro testing of In-Ceram Alumina and Spinell ceramic," *International Journal of Prosthodontics*, vol. 10, no. 5, 1997.

[14] T. Jain, A. Porwal, B. R. Bangar, S. B. Randive, K.nP. Vaishnav, K. Walkar, and A. S. Nayyar, "Computer-aided design and computer-aided manufacturing ceramic biomaterials in dentistry: Past to present," *Journal of Dental and Allied Sciences*, vol. 7, no. 1, p. 18, 2018.

[15] M. Fradeani, A. Aquilano, and M. Corrado, "Clinical experience with in-ceram spinell crowns: 5-year follow-up," *International journal of periodontics & restorative dentistry*, vol. 22, no. 6, 2002.

[16] E. O. Einset. "Capillary infiltration rates into porous media with applications to silcomp processing," *Journal of the American Ceramic Society*, vol. 79, no. 2, pp. 333-338, 1996.

[17] D. Y. Lee, D. J. Kim, B. Y. Kim, and Y. S. Song, "Effect of alumina particle size and distribution on infiltration rate and fracture toughness of alumina–glass composites prepared by melt infiltration," *Materials Science and Engineering: A*, vol. 341, no. 1-2, pp. 98-105, 2003.

[18] S. Shi, Q. Zhang, H. Wang, and Y. Li, "$La_2O_3$–$Al_2O_3$–$SiO_2$ glass-infiltrated 3Y-TZP all-ceramic composite for the dental restorative application". *Progress in Natural Science: Materials International*, vol. 22, no. 3, pp. 224-230, 2012.

[19] Z. Yang, Q. Jin, J. Ma, Y. Tong, X. Wang, R. Du, and S. Wang, "Glass infiltration of gel cast zirconia-toughened alumina ceramics for dental restoration," *Ceramics International*, vol. 38, no. 6, pp. 4653-4659, 2012.

[20] M. B. Berger, "The importance and testing of density/porosity/permeability/pore size for refractories," in *The Southern African Institute of Mining and Metallurgy Refractories Conference*, pp. 101-116, 2010.

[21] D. D. L. Chung, "Polymer-matrix composites: Structure and processing," *Carbon Composites*, pp. 161-217, 2017.

[22] D. Yang, Y. Zhang, X. Song, Y. Chen, Z. Shen, and C. Yang, "Effects of sintering temperature and holding time on porosity and shrinkage of glass tubes," *Ceramics International*, vol. 42, no. 5, pp. 5906-5910, 2016.

[23] S. J. Lee, M. K. Waltraud, and H. M. Kim, "Shrinkage-free, alumina–glass dental composites via aluminum oxidation," *Journal of the American Ceramic Society*, vol. 80, no. 8, pp. 2141-2147, 1997.

[24] V. Bougiouri, R. Voytovych, N. Rojo-Calderon, J. Narciso, and N. Eustathopoulos, "The role of the chemical reaction in the infiltration of porous carbon by NiSi alloys," *Scripta materialia*, vol. 54, no. 11, pp. 1875-1878, 2006.

[25] S. Wan, X. Tang, Y. Sun, G. Zhang, J. You, and P. Fu, "Raman spectroscopy and density functional theory analyses of the melt structure in a $Li_2B_4O_7$ crystal growth system," *Cryst Eng Comm*, vol. 16, no. 15, pp. 3086-3090, 2014.

[26] N. Van Minh, and I. S. Yang. "A Raman study of the cation-disorder transition temperature of natural $MgAl_2O_4$ spinel," *Vibrational Spectroscopy*, vol. 35, no. 1-2, pp. 93-96. 2004.

[27] S. Li, D. Xu, H. Shen, J. Zhou, and Y. Fan, "Synthesis and Raman properties of magnesium borate micro/nanorods," *Materials Research Bulletin*, vol. 47, no. 11, pp. 3650-3653, 2012.

[28] A. K. Yadav, and P. Singh. "A review of the structures of oxide glasses by Raman spectroscopy," *RSC advances*, vol. 5, no. 83, pp. 67583-67609, 2015.

[29] J. Seuba, S. Deville, C. Guizard, and A.J. Stevenson, "Mechanical properties and failure behavior of unidirectional porous ceramics," *Scientific reports*, no. 6, no. 1, pp. 1-11, 2016.